Reconstruction performance for image transmission through multimode fibers*

HU Shicheng[1], LIN Wei[1], LIU Haifeng[1], ZHU Yan[2], YANG Ling[2], and JIN Song[2]**

1. Tianjin Key Laboratory of Micro-scale Optical Information Science and Technology, Institute of Modern Optics, Nankai University, Tianjin 300350, China

2. Foreign Cooperation Projects Department, PetroChina Dagang Oilfield Company, Tianjin 300280, China

(Received 8 November 2022; Revised 21 November 2022)

Due to the applications in the fields of optical communication, neuronal imaging, and medical endoscopic imaging, the study of multimode fiber (MMF) wavefront transmission is crucial for image reconstruction and wavefront generation in user terminals. State of art studies in this area focus on high-quality image reconstruction and wavefront shaping. Besides the way of imaging reconstruction, the performances of image reconstruction and wavefront shaping are also dependent on system and environment parameters. This paper numerically analyzes the influence of key factors, such as the numerical aperture (*NA*) of the near-end objective lens of the MMF imaging system, the charge coupled device (CCD) noise of the acquired image, and the ambient temperature at close distances. This work would help to the optimization of the MMF-based imaging system and provide a theoretical basis for potential applications in optical communication systems, neuron imaging and endoscopic diagnosis.

Document code: A **Article ID:** 1673-1905(2023)04-0235-7

DOI https://doi.org/10.1007/s11801-023-2186-y

With the increasing demand of transmission traffic in the fields of modern telecommunications[1] and medical endoscopic imaging[2], multimode fiber (MMF) is considered as one type of important optical medium to carry information owing to its low cost and large transmission capacity. Especially in the area of medical endoscopic imaging, MMFs greatly enhance the data collection ability and high-resolution imaging could be achieved without the need of fiber bundles, which makes fiber-based endoscope more compact and portable for practical use[3,4].

However, several issues still hinder the widespread applications of MMFs. The most critical one is the interference between different guided modes in MMFs, which distorts the input wavefront of the light projected on proximal side into the specklegram on the distal side[5]. To achieve wavefront reconstruction or low-distortion imaging based on laser specklegram, various schemes, including phase conjugation[6,7], digital holography[8], machine learning[9,10], transmission matrix (TM)[11-14], have been proposed to achieve image reconstruction based on specklegram analysis.

Among the above schemes, the TM method was the most widely used, as the TM well describes the relationship between the input and output fields of optical fibers. Once measured, the image can be processed and reconstructed by using the output specklegram and TM. Different from the conventional TM method, CARAMAZZA et al[13] achieved reconstruction of natural color images by setting up a model based on inverse complex TM without the requirement of several layers of deep learning. Recently, FAN et al[14] improved the image reconstruction quality by using polarization-dependent transmission matrix, which describes polarization evolution process of the light propagating through the medium. With the help of the TM, one can achieve the image reconstruction with better fidelity and obtain the target wavefront at the fiber output. Besides, the reconstruction of original image and wavefront is also affected by the settings of the MMF-based image/wavefront transmission system, such as the objective numerical aperture (*NA*), the charge coupled device (CCD) noise and the ambient temperature. Numerical simulations would help to determine the appropriate system parameters and evaluate the performance of the MMF-based image transmission system.

In this paper, we investigate wavefront transmission through MMFs and numerally analyze the image reconstruction performance based on TM method in the short-distance transmission system. Different from the

* This work has been supported by the National Natural Science Foundation of China (Nos.11904180, 11904262, 11774181 and 61875091), the Natural Science Foundation of Tianjin (Nos.19JCYBJC16700, 20JCQNJC01480 and 21JCQNJC00210), and the Science and Technology on Electronic Test & Measurement Laboratory (No.6142001200302).

** E-mail: 016045@nankai.edu.cn

onventional TM method, we use a complex transmission matrix to reconstruct the wavefront that serves as both of the amplitude and phase terms of the specklegrams acquired at the output of MMFs. We discuss the impact of objective *NA* at proximal end, the noise of acquired images, as well as the environmental temperature on the image reconstruction performance. This work helps to optimize the MMF-based imaging system and provides a theoretical basis for applications in optical communication systems, neuron imaging and endoscopic diagnosis.

The deterministic scattering process inside the MMFs can be characterized by using TM. The TM can be obtained by measuring the output specklegram of each input point with unit amplitude and zero phase. The specklegram for the point $p(\xi, \eta)$ can be written as $PS(x, y; \xi, \eta)$, which is named as point-related specklegram. Then, as the input light with wavefront (ξ, η) propagates through the MMFs, the output light field $E(x, y)$ can be expressed by

$$E(x,y)=\sum\nolimits_{\xi,\eta} PS(x,y;\xi,\eta)\,O(\xi,\eta). \quad (1)$$

Then, the specklegrams between each two points can be considered independently, i.e., the correlation coefficient between them is approximately zero. Thus, the input wavefront can be obtained by calculating the correlation coefficient between the output specklegram and each point-related specklegram as

$$O(\xi,\eta)=\mathrm{corr}[E(x,y),PS(x,y;\xi,\eta)]. \quad (2)$$

Note that the amplitude and phase information are obtained after two-dimensional Fourier transform and unwrapping of the image respectively. Since the system settings have the same impact on the reconstruction performance of wavefront and images, our concern is focused on the image reconstruction. To evaluate the image quality of the reconstructed images, we introduce a few parameters[15], including the mean absolute error (*MAE*), structural similarity index measure (*SSIM*), peak signal to noise ratio (*PSNR*), and Pearson correlation coefficient (*PCC*), to measure the similarity between the reconstructed image $\boldsymbol{Y}$ and the original image $\boldsymbol{X}$. And we have

$$MAE(y_i,\hat{y}_i)=\frac{1}{n}\sum\nolimits_{i=1}^{n}\left|y_i-\hat{y}_i\right|, \quad (3)$$

where y_i and $\hat{y}_i$ represent the true value and the observed value, respectively.

$$SSIM(\boldsymbol{X},\boldsymbol{Y})=\frac{(2\mu_X\mu_Y+C_1)(2\sigma_{XY}+C_2)}{(\mu_{X^2}+\mu_{Y^2}+C_1)(\sigma_{X^2}+\sigma_{Y^2}+C_2)}, \quad (4)$$

where $\mu_X\sigma_{X^2}$ and σ_{XY} represent the mean value variance and covariance of images $\boldsymbol{X}$ and $\boldsymbol{Y}$, and C_1 and C_2 are constants.

$$MSE(\boldsymbol{X},\boldsymbol{Y})=\frac{1}{H\times W}\sum\nolimits_{i=1}^{H}\sum\nolimits_{j=1}^{W}[\boldsymbol{X}(i,j)-\boldsymbol{Y}(i,j)]^2, \quad (5)$$

$$PSNR(\boldsymbol{X},\boldsymbol{Y})=10\log_{10}[\frac{(2^n-1)^2}{MSE}], \quad (6)$$

where *MSE*, *H* and *W* represent the mean square error, height and width of image, *n* is the number of bits per pixel, and the number of gray levels is 256. The unit of *PSNR* is dB, and the image distortion becomes stronger when this value is larger.

$$PCC=\frac{\mathrm{cov}(\boldsymbol{X},\boldsymbol{Y})}{\sigma_X\sigma_Y}, \quad (7)$$

where cov($\boldsymbol{X}$, $\boldsymbol{Y}$) is the covariance between image $\boldsymbol{X}$ and image $\boldsymbol{Y}$, and σ_X and σ_Y refer to their respective standard deviations. These parameters are sued to evaluate the image construction performance in successive sections.

The model of MMF-based transmission system for image reconstruction is shown in Fig.1. The input light from a laser source (LS) is launched into a 0.1-m-long commercially available step-index MMF with core/cladding diameters of 100 μm/125 μm and refractive indices of 1.485 3/1.471 8, respectively. The input patterns are loaded onto a spatial light modulator (SLM), and CCD1 captures the modulated beam. CCD2 is placed at the output of MMFs, after mirrors (M), lens (L) and beam splitters (BSs), to capture the transmission light, which results from the interference of the specklegram and the input light. The input light is obliquely interfered with the specklegram for interrogation of the phase information. The transmission wavefront information could be retrieved by adjusting the SLM according to the phase feedback. The sizes of the image and specklegram are 41×41 and 205×205, respectively. The pixel-to-pixel distance is set to 1.6 μm. The dashed rectangle gives the region of interest in our simulation. Note that the *NA* of Obj.1 (defined as the obj. *NA*) and noise of CCD2 (defined as the CCD noise) are both taken into account. Besides, environmental temperature variations are also considered in our numeral analysis by temperature control chamber.

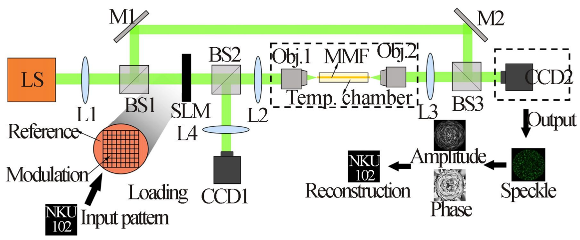

Fig.1 Simulation system setup

Before the simulation process, the performance of the complex transmission matrix in image reconstruction needs to be validated. In Fig.2, we select the handwritten digits 0 to 9 in the MINST datasets as ground truth (GT), and the original image is reconstructed according to the amplitude and phase information of the output specklegram. The obj. *NA* is set to 0.45 without noise in this case. Fig.2 indicates that the average values of the *MAE*, *SSIM*, *PSNR*, and *PCC* of the ten reconstructed images are 0.037 3, 0.947 8, 22.724 dB, and 0.925 4, respectively, representing the small error, structural similarity of more than 94%, less distortion, and strong positive correlation between the recovered and the original images. These results show good image reconstruction performance, which could be reflected by the obj. *NA* and CCD noise variance (*Var*).

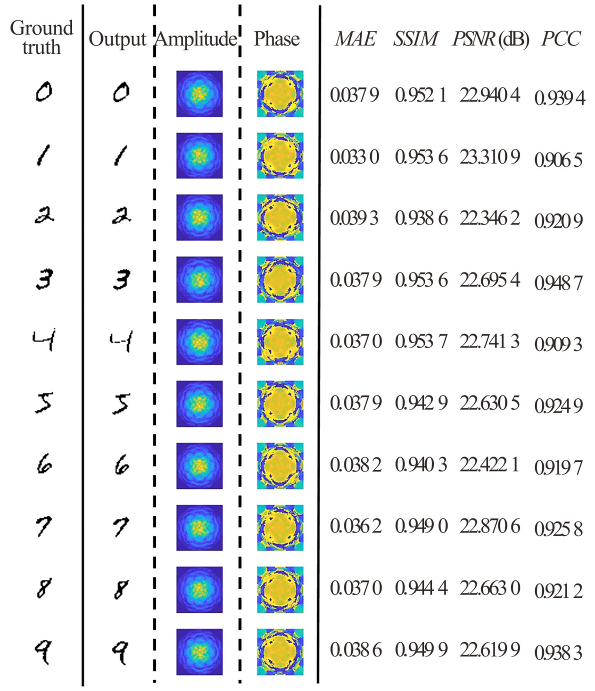

Fig.2 Reconstruction of handwritten digits

To investigate the influence of obj. *NA* on the MMF-based wavefront transmission system, the grayscale image of Moon and the binary image of NKU102 are adopted in our simulation for obj. *NAs* ranging from 0.1 to 0.9. Fig.3 shows the image of Moon projected onto the fiber facet, which serves as the original target image GT. All of the reconstructed images are converted into the grayscale ones to economize the calculation resources. Compared with case of obj. *NA* of 0.1, the reconstruction image when obj. *NA* is 0.9 has a higher resolution, sharper edge texture, and the clearer features of lunar landform, along with the more sophisticated amplitude and phase specklegrams. Note that the lower right corner value represents *PCC*.

For *MAE*, in Fig.4, its value rapidly decays from its original value of about 0.1 to 0.025 6 as obj. *NA* gradually increases from 0.1 to 0.4, showing a reduction in the absolute error while an increase in reconstruction accuracy. The value of *SSIM* increases from 0.541 1 to 0.814 2 as obj. *NA* increases from 0.1 to 0.3, showing that the geographic structure of the Moon and its occlusion strongly resembles GT. However, as obj. *NA* increases, the maximum value of 0.965 9 is obtained when obj. *NA* is 0.6 and then decreases to 0.938 7 when obj. *NA* is 0.9, which is caused by the jagged edges of the reconstructed image. The results show that *SSIM* is improved by 78.5%. Finally, the approximately doubled *PSNR* value, from 16.997 6 dB to 32.388 1 dB, considerably improves the resolution of reconstructed images. In general, more propagation modes due to larger obj. *NA* contributes to better image reconstruction effects. In practice, however, the crucial issue is to choose the most suitable obj. *NA* under the limitation of lens size. Our model obtains an *SSIM* of more than 0.9 and a *PSNR* beyond 27 dB when obj. *NA* is 0.4, which means that high performance reconstruction is feasible in MMF transmission system.

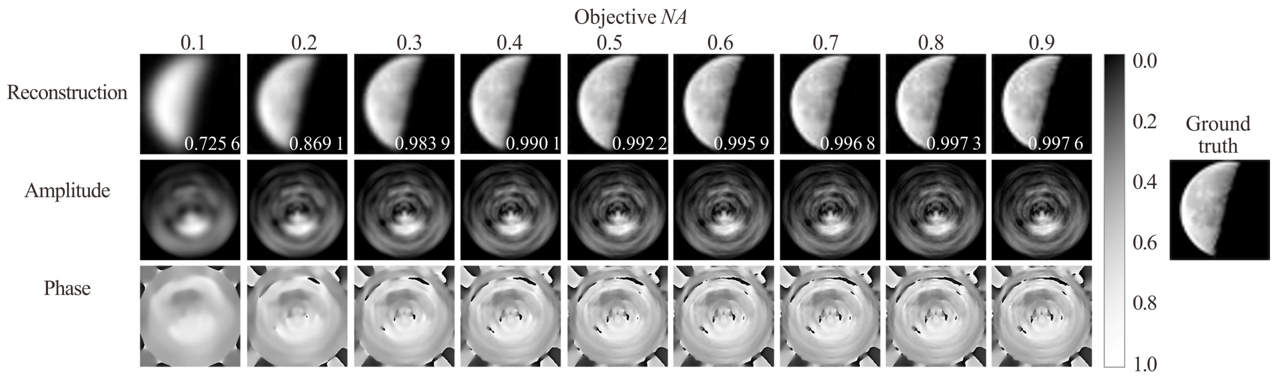

Fig.3 Reconstruction of the grayscale image Moon

For the image NKU102, the obj. *NA* has a significant impact on the reconstruction quality in the same simulation conditions, as shown in Fig.5 and Fig.6. The reconstruction quality gradually approaches GT, and *PCC* varies from 0.519 0 to 0.977 6 with the increase of obj. *NA*. The large obj. *NA* helps to improve the resolution of the corner details of the letters and yields high correlation, which validates the reconstruction ability of our model. It should be noted that the reconstruction image is much clearer in comparison with the initially blurred mask for the obj. *NA* range from 0.1 to 0.5, and its *SSIM* value increases from 0.114 6 to about 0.813 4. The above results show our model also has good performance in wavefront reconstruction for both of grayscale and binary images. Further, based on this MMF transmission model, the most suitable commercial objective lens selection can be provided for different types of targets, e.g., obj. *NA* of 0.4 for grayscale images and obj. *NA* of 0.5 for binarized images.

In the next section, to evaluate the impact of different types of CCD noises on reconstruction of the grayscale Moon image and the binary NKU102 image, typical noises, such as Gaussian, mean, and salt pepper noises, are added to simulate the practical situation. Here, the obj. *NA* of the system is set to 0.4. Simulation results for the noise variance ranging from 0.001 to 0.3 are shown in Fig.7, and Fig.8 gives quantitative evaluations of reconstruction performance. As noise variance increases, irregular spots emerge in the specklegrams captured by the CCD, which results in some decrease in the reconstruction fidelity. This can be seen from the graininess in the salt pepper noise in Fig.7. The sampling points between the reconstruction and the GT have a strong correlation, which leads to the larger values and smaller deviations of *PCC*.

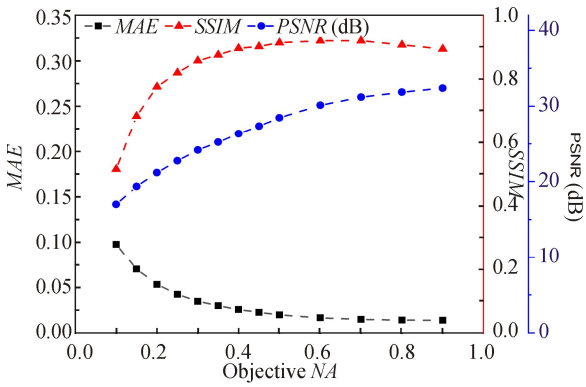

Fig.4 Evaluation of the grayscale image Moon

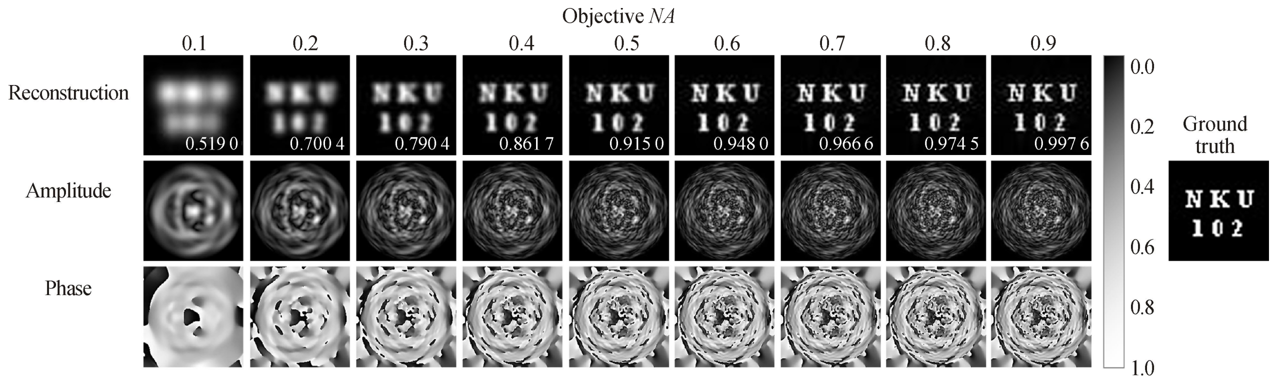

Fig.5 Reconstruction of the binary image NKU102

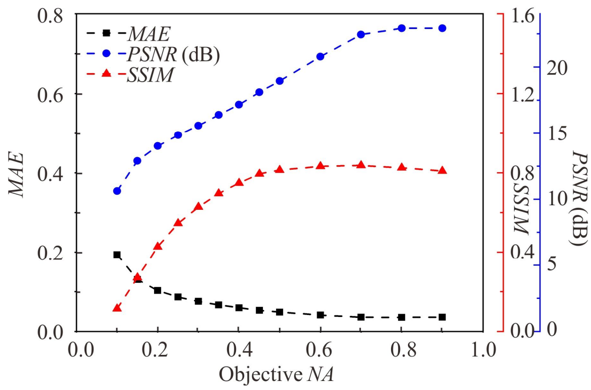

Fig.6 Evaluation of the binary image NKU102

For *MAE* in Fig.8, all of the three kinds of noises approximately linearly increasing indicate that the absolute error of the sampling points would rapidly increase and result in a slight distortion. As to structural similarity, the *SSIM* values of Gaussian and mean noises approximately linearly decrease from 0.948 0 to 0.669 5, and 0.947 2 to 0.737 0 with slopes of 0.94 and 0.73, respectively, while the randomly distributed graininess of salt pepper noise is inconsistent with the internal structure and edge of the Moon. With the presence of salt pepper noise, *SSIM* dropped rapidly and finally decreased to 0.619 9 when the *Var* is 0.3, showing a more than 1/3 decrease in structural similarity. Finally, the *PSNR* shows the smallest change among the three types of noises. Compared

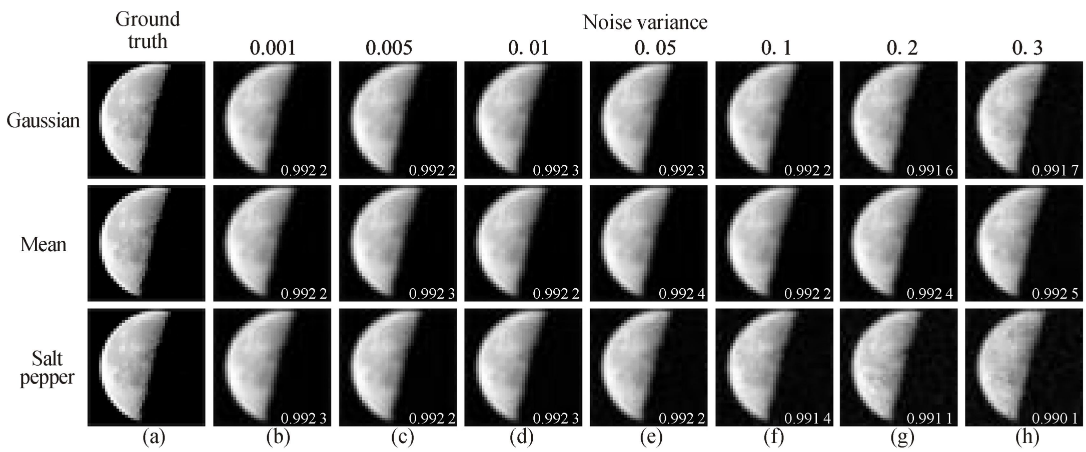

Fig.7 Reconstruction of Moon with noises

with *MAE* and *SSIM*, the *PSNR* shows the lowest value of 24.800 1, which means that the *SNR* of the reconstructed pixel value is the least affected by the CCD noise and thus leads to high similarity to the view of human eye and high *PCC* of the reconstructed image under different noises *Var*. Generally speaking, salt pepper noise has the most significant impact on image reconstruction quality, and the *SSIM* and *MAE* values both lower the reconstruction quality by more than 1/3. These results indicate that different types of CCD noises have different degrees of impact on reconstruction of grayscale images, and provide a basis for experimental verifications.

It can be found that the reconstructed binary images with noises obviously become blurred in Fig.9, while the image shape is still recognizable. As the variance increases from 0.001 to 0.3, the average *PCCs* of Gaussian noise, mean noise, and salt pepper noise tend to be 0.894 8, 0.894 7 and 0.895 7, respectively, which proves that the quality of image reconstruction is difficult to perceive by human eyes. Furthermore, the reconstructed images with salt pepper noise show the largest pixel value error due to the presence of stains in Fig.10. The values of the *SSIM* indicate that the detailed image structures significantly attenuate and are no longer visible to the human eyes. In all, the three types of noises have significant impacts on the pixel value error of the reconstructed images, but do not much affect the *PSNR*. Salt pepper noise exhibits the most severe impact due to the randomly distributed stains.

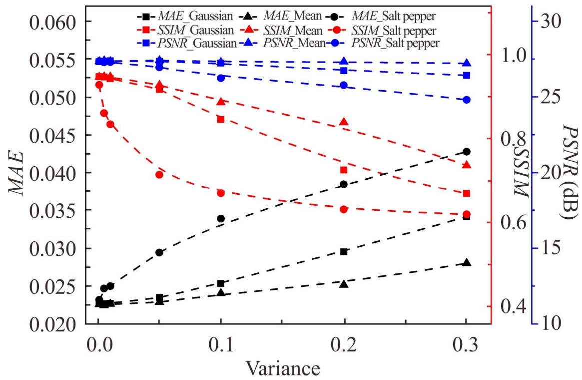

Fig.8 Evaluation of Moon with noises

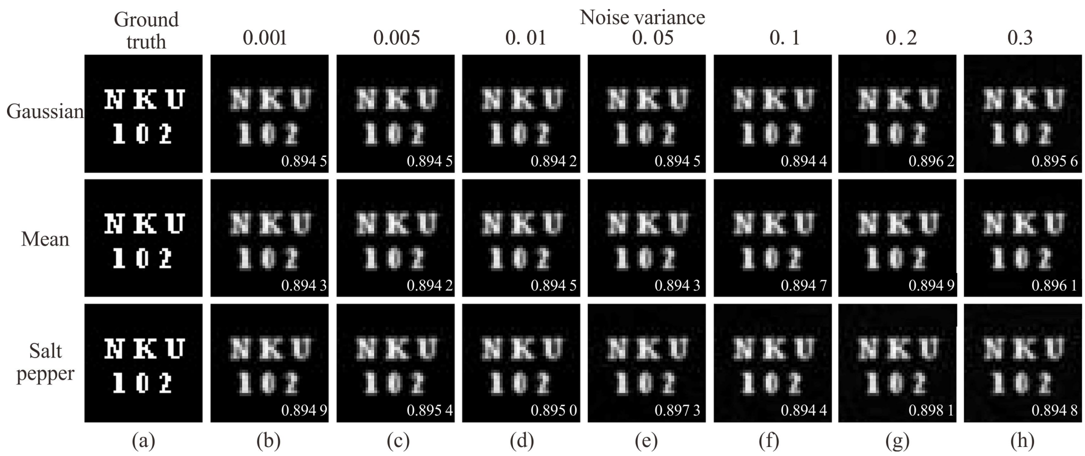

Fig.9 Reconstruction of NKU102 with noises

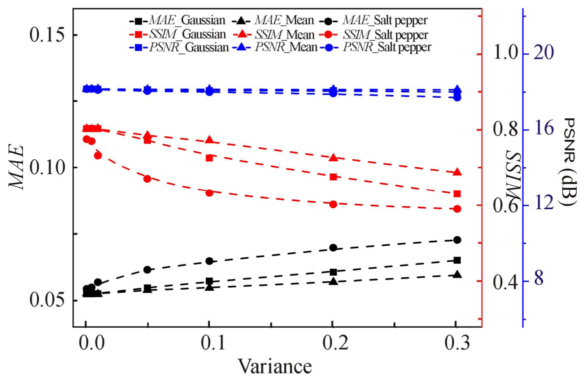

Fig.10 Evaluation of NKU102 with noises

Additionally, the impact of ambient temperature has also been investigated, as shown in Fig.11. Fig.12 and Fig.13 respectively show the temperature responses of the grayscale image Moon and the binary image NKU102 based on three types of evaluation methods for the temperature change from 0 to 15 °C (initial room temperature is 25 °C). The obj. *NA* of the system is 0.4 and the specklegrams can be obtained without any noise. In Fig.12, the values of *MAE*, *SSIM*, and *PSNR* are changed of 0.000 2, 0.000 5 and 0.523 4, respectively. Similarly, in Fig.13, these changes are 0.004 6, 0.038 5 and 0.678 0, respectively. The results indicate that our proposed model is temperature insensitive for image transmission through 0.1-m-long MMFs, which could be attributed to the fact that the phase difference between the eigen modes accumulated over such a transmission distance changes a little with the variation of external temperature. As a result, the amplitude and phase of each-point related specklegram do not change much, so that the image reconstruction quality is not obviously affected by the variation of environmental temperature at centimetre-level transmission distance.

Furthermore, the reconstructed grayscale and binary images and their evaluation values for different lengths of MMFs are shown in Fig.14 (at dT of 10 °C in Fig.11, i.e., 35 °C) and Tab.1 respectively. It can be seen that the strong dispersion in the case of long-distance transmission through MMFs results in severe distortion in the reconstructed images. Therefore, a tradeoff between image reconstruction quality and length of MMFs is a topic that should be further investigated in our future study.

We have established a numerical model for the analysis of the wavefront transmission through MMFs and investigated the influences of obj. NA and CCD noises on the image reconstruction performance. By optimizing

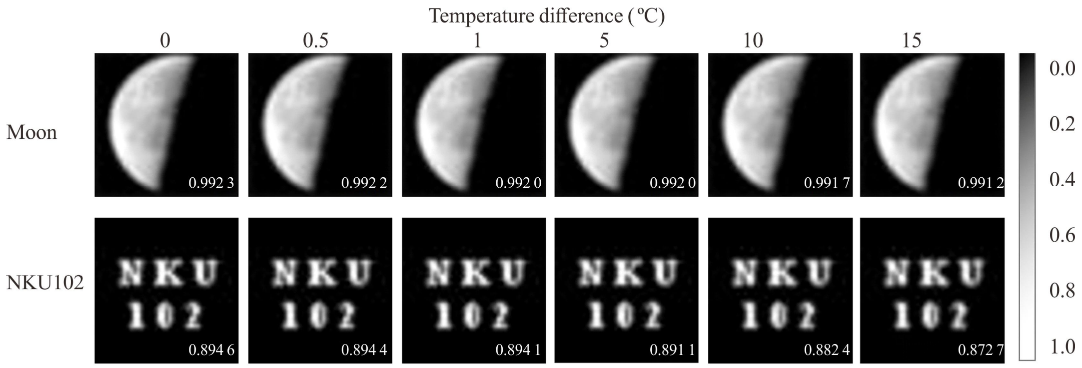

Fig.11 Temperature variations compared to 25 °C

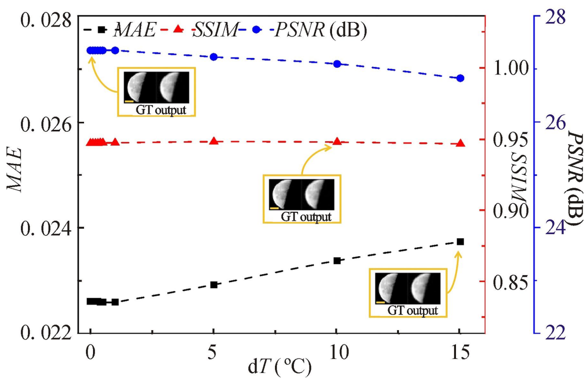

Fig.12 Impacts of temperature on Moon

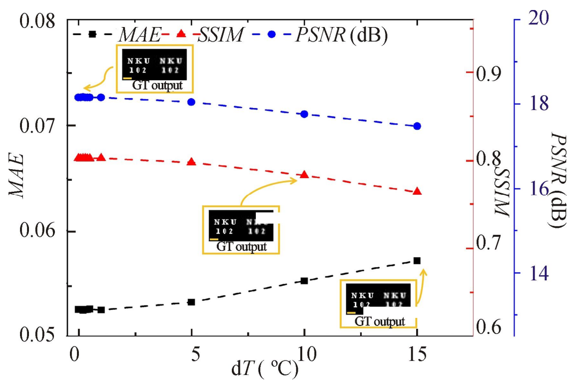

Fig.13 Impacts of temperature on NKU102

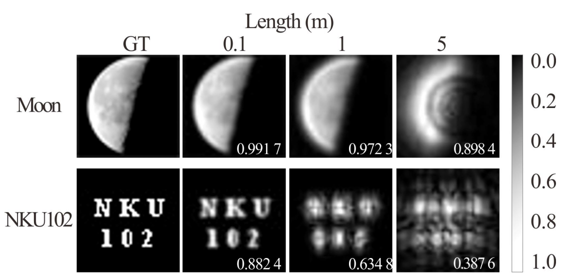

Fig.14 Length variations of MMFs

Tab.1 Evaluation of different lengths of MMFs

Length	*MAE*		*SSIM*		*PSNR* (dB)	
(m)	Moon	NKU102	Moon	NKU102	Moon	NKU102
0.1	0.023 4	0.055 24	0.947 9	0.783 25	27.093 2	17.763 9
1	0.049 0	0.116 51	0.797 0	0.296 83	21.558 3	13.307 9
5	0.112 8	0.218 99	0.306 2	0.039 46	16.168 6	10.591 6

system parameters, high-fidelity wavefront transmission and image reconstruction based on MMFs can beachieved. Better image reconstruction quality would benefit to endoscopic applications for the ease of detecting lesions. And our proposed MMF-based image reconstruction technique can be also applied in vivo imaging of biological tissues. In our future study, we will focus on setting up an experimental platform and calibrating the experimental parameters according to the numerical simulation results.

Statements and Declarations

The authors declare that there are no conflicts of interest related to this article.

References

[1] RICHARDSON D J, FINI J M, NELSON L E. Space-division multiplexing in optical fibres[J]. Nature photonics, 2013, 7(5): 354-362.

[2] FLUSBERG B A, COCKER E D, PIYAWATTANAMETHA W, et al. Fiber-optic fluorescence imaging[J]. Nature methods, 2005, 2(12): 941-950.

[3] ČIŽMÁR T, DHOLAKIA K. Exploiting multimode waveguides for pure fibre-based imaging[J]. Nature communications, 2012, 3(1): 1027.

[4] TURTAEV S, LEITE I T, ALTWEGG-BOUSSAC T, et al. High-fidelity multimode fibre-based endoscopy for

deep brain in vivo imaging[J]. Light-science & applications, 2018, 7：92.
[5] DI LEONARDO R, BIANCHI S. Hologram transmission through multi-mode optical fibers[J]. Optics express, 2011, 19(1)：247-254.
[6] PAPADOPOULOS I N, FARAHI S, MOSER C, et al. Focusing and scanning light through a multimode optical fiber using digital phase conjugation[J]. Optics express, 2012, 20(10)：10583-10590.
[7] CZARSKE J W, HAUFE D, KOUKOURAKIS N, et al. Transmission of independent signals through a multimode fiber using digital optical phase conjugation[J]. Optics express, 2016, 24(13)：15128-15136.
[8] PLOSCHNER M, CIZMAR T. Compact multimode fiber beam-shaping system based on GPU accelerated digital holography[J]. Optics letters, 2015, 40(2)：197-200.
[9] BORHANI N, KAKKAVA E, MOSER C, et al. Learning to see through multimode fibers[J]. Optica, 2018, 5(8)：960-966.
[10] PLÖSCHNER M, TYC T, ČIŽMÁR T. Seeing through chaos in multimode fibres[J]. Nature photonics, 2015, 9(8)：529-535.
[11] ZHAO T, OURSELIN S, VERCAUTEREN T, et al. Seeing through multimode fibers with real-valued intensity transmission matrices[J]. Optics express, 2020, 28(14)：20978-20991.
[12] LI S, SAUNDERS C, LUM D J, et al. Compressively sampling the optical transmission matrix of a multimode fibre[J]. Light-science & applications, 2021, 10(1)：88.
[13] CARAMAZZA P, MORAN O, MURRAY-SMITH R, et al. Transmission of natural scene images through a multimode fibre[J]. Nature communications, 2019, 10(1)：2029.
[14] FAN W, CHEN Z, YAKOVLEV V V, et al. High-fidelity image reconstruction through multimode fiber via polarization-enhanced parametric speckle imaging[J]. Laser photonics review, 2021, 15(5)：2000376.
[15] TANG P, ZHENG K, YUAN W, et al. Learning to transmit images through optical speckle of a multimode fiber with high fidelity[J]. Applied physics letters, 2022, 121(8)：081107.